Characterizing, Mitigating, and Comparing the Along-Scanline Noise in Fengyun-3 Series Microwave Humidity Sounders (MWHSs)

Lijian Zhu, Zhengkun Qin, Jinzhong Min, and Ming Xue

***Abstract*— Chinese Fengyun 3 (FY-3) polar-orbiting satellites carry Microwave Humidity Sounders (MWHSs), including MWHS and MWHS-2 which are on board FY-3A/B and FY-3C/D, respectively. Understanding the quality of MWHS data is important for data assimilation and other applications. Examination of observed and simulated brightness temperatures and comparison with those of the NOAA-18 Microwave Humidity Sounder (MHS) reveal that the FY-3C MWHS-2 observations contain significant along-scanline noise. Similar noise exists in the humidity sounder data from FY-3 series satellites. In this study, the principal component analysis (PCA) method is used to identify and characterize the along-scanline noise, and a noise filter is also applied to the FY-3 series MWHS data by combining a PCA with a five-point smoother. The observation minus background or O-B biases of MWHS channels vary more smoothly with scan position after applying the filter, indicating that the along-scanline noise has been effectively reduced. Comparisons of O-B biases among all four FY-3 MWHS instruments show that biases for different channels have different asymmetric scan-angle features. As for along-scanline noise, FY-3A MWHS has the largest noise: 0.16, 0.27, and 0.89 K for channels 3–5, respectively. Noise in the FY-3D humidity channels is the smallest, of the order of 0.06–0.07 K. The along-scanline noise is also strongly correlated between channels.**

***Index Terms*— Along-scanline noise, Fengyun-3, microwave humidity sounder, principal component analysis (PCA).**

I. Introduction

SINCE the launch of the first polar-orbiting National Oceanic and Atmospheric Administration NOAA-15 satellite carrying an Advanced Microwave Sounding Unit B (AMSU-B), Microwave Humidity Sounder data have been playing an important role in numerical weather prediction (NWP). Microwave Humidity Sounders (MWHS) are sensitive to atmospheric temperature and humidity; therefore, they can be used to monitor atmospheric parameters associated with severe convective weather systems, such as tropical cyclones and thunderstorms, as well as providing vertical profiles of atmospheric water vapor globally under nearly all weather conditions, and such data are important for data assimilation (DA). MWHS data are effective supplements to conventional water vapor measurements, such as those from traditional radiosonde observations. Prior researches have also shown positive impacts with direct assimilating radiance from humidity sounders on improving the analysis and the prediction of mid–upper tropospheric wind, temperature, and humidity [1]–[4].

On May 27, 2008 and November 5, 2010, China launched two polar-orbiting meteorological satellites, Fengyun (FY) 3A and 3B. The first generation of MWHS was among the instruments on these two satellites [5]. MWHS is similar to the AMSU-B/MHS (Microwave Humidity Sounder) on board the NOAA and the European Organization for the Exploitation of Meteorological Satellite (EUMETSAT) operational polar-orbiting satellites. The second-generation satellites of the FY-3 series, FY-3C, and FY-3D, were successfully launched on September 23, 2013 and November 15, 2017, carrying an updated version of MWHS, known as MWHS-2. Two extra sounding channels near 183 GHz were added to MWHS-2, similar to the Advanced Technology Microwave Sounder (ATMS) on board the Suomi National Polar-Orbiting Partnership (SNPP) but with different polarizations. In addition, MWHS-2 has eight new sounding channels centered around the 118-GHz oxygen band. This is the first time that these channels have been applied to polar-orbiting satellites.

Since the launch of FY-3A, MWHS data have been widely used in NWPs. Precipitation and atmospheric temperature and humidity profiles can be retrieved from the MWHS observations [6], [7]. Many studies have also focused on cloud parameter estimation (e.g., ice water path (IWP) and cloud liquid water) and cloud detection [8]–[11]. In addition, the improvement in assimilating MWHS data into short-term weather forecasting has been well demonstrated [12]–[14]. The European Centre for Medium-Range Weather Forecasts (ECMWF)

Manuscript received May 11, 2020; revised August 1, 2020 and November 11, 2020; accepted November 30, 2020. Date of publication January 5, 2021; date of current version December 3, 2021. This work was supported in part by the National Key Research and Development Program of China under Grant 2018YFC1507302, in part by the National Natural Science Foundation of China under Grant 41805076, and in part by the Nanjing Joint Center of Atmospheric Research Program under Project NJCAR2018ZD01. *(Corresponding author: Zhengkun Qin.)*

Lijian Zhu and Jinzhong Min are with the Key Laboratory of Meteorological Disaster of Ministry of Education (KLME), Nanjing University of Information Science and Technology, Nanjing 210044, China, and also with the Collaborative Innovation Center on Forecast and Evaluation of Meteorological Disasters, Nanjing University of Information Science and Technology, Nanjing 210044, China.

Zhengkun Qin is with the Center of Data Assimilation for Research and Application, Nanjing University of Information Science and Technology, Nanjing 210044, China (e-mail: qzk_0@nuist.edu.cn).

Ming Xue is with the Center for Analysis and Prediction of Storms, University of Oklahoma, Norman, OK 73019 USA.

Digital Object Identifier 10.1109/TGRS.2020.3043310

has been routinely assimilating FY-series MWHS observations into its operational forecasting system since September 2014 [15]–[18]. Its results show an improvement in both short-range and long-range forecasts, even with relatively large MWHS instrumental noise.

To better utilize the MWHS data for DA and other applications, a better understanding of their bias characteristics is necessary. Calibration studies of MWHS and MWHS-2, and evaluations of MWHS data quality indicate that their in-orbit performances are comparable to similar instruments on board other platforms [19]–[22]. However, by comparing model-simulated brightness temperatures with MWHS measurements, Zou *et al.* [23] found a line shape cohesive noise along the scanline in the FY-3B MWHS sounding channels. Although this noise was first found in FY-3B MWHS, less attention was paid to the MWHS on board other FY polar-orbiting satellites. In addition, no comparison studies of their bias characteristics before and after removing the noise have been performed. In this study, the along-scanline noises in the MWHS data from the four FY-3 satellites are compared, and the bias characteristics of the MWHS data are analyzed to provide some reference for the improvement in MWHS instruments and the assimilation of MWHS data into NWP models.

This article is organized as follows. The MWHS instrument characteristics and the radiative-transfer model (RTM) used in this article are briefly introduced in Section II. In Section III, the scan-angle dependence of O-B biases for FY-3C MWHS-2 and NOAA-18 MHS is compared to help reveal the along-scanline noise in MWHS-2. The principal component analysis (PCA) approach combined with a five-point smoother is used to characterize and filter the noise; then along-scanline noise characteristics and comparisons of the noises among the four MWHSs on the FY-3 satellites are presented in Section IV. Finally, in Section V, a summary and conclusions are provided.

II. Instrument Characteristics and RTM

A. MWHS and MWHS-2 Instrument Characteristics

In this study, we use Level-1C MWHS and MWHS-2 radiance data provided by the National Satellite Meteorological Center (NSMC) (http://satellite.nsmc.org.cn/PortalSite/Data/Satellite.aspx). Four weeks of data, i.e., November 1–7, 2008 for FY-3A MWHS, April 2–8, 2011 for FY-3B MWHS, November 1–7, 2013 for FY-3C MWHS-2, and June 1–7, 2018 for FY-3D MWHS-2, are used for the characterization and mitigation of the along-scanline noise in those instruments.

Both MWHS and MWHS-2 are cross-track scanning microwave radiometers with a swath width of 2700 km and a scan coverage of 53.35° with respect to the nadir. Each scan line has a total of 98 fields of view (FOVs) and is completed in 8/3 s. The detailed characteristics of MWHS and MWHS-2 are provided in Table I. The MWHS on board FY-3A/B has five channels, including two window channels at 150 GHz with different polarizations and three humidity sounding channels at approximately 183 GHz (near the water vapor absorption line) designed to provide information on humidity at different heights in the atmosphere. Each MWHS channel has a horizontal resolution of 16 km at the nadir. The MWHS-2 shown on FY-3C/D has 15 channels. Channels 1 and 10 are two window channels at 89 and 150 GHz, which are sensitive to surface parameters and precipitation. Channels 2–9 sample around the 118.75-GHz oxygen line. These channels are strongly sensitive to both atmospheric temperature and humidity. Two new channels were added to the MWHS-2 183-GHz water vapor line with frequencies at 183.3 $\pm$ 1.8 and 183.31 $\pm$ 4.5 GHz. The resolution of MWHS-2 is 32 km at the nadir for channels 1–9 and 16 km for channels 10–15. The noise equivalent differential temperature (NEdT) values range from 1 to 3.6 K for all MWHS-2 channels.

TABLE I
MWHS and MWHS-2 Instrument Characteristics

Channel Number		Frequency (GHz)		NEΔT (K)	
MWHS-2	MWHS	MWHS-2	MWHS	MWHS-2	MWHS
1	1	89(V)	150(V)	1	0.9
2	-	118.75±0.08(H)	-	3.6	-
3	-	118.75±0.2(H)	-	2	-
4	-	118.75±0.3(H)	-	1.6	-
5	-	118.75±0.8(H)	-	1.6	-
6	-	118.75±1.1(H)	-	1.6	-
7	-	118.75±2.5(H)	-	1.6	-
8	-	118.75±3.0(H)	-	1	-
9	-	118.75±5.0(H)	-	1	-
10	2	150(V)	150(H)	1	0.9
11	3	183.31±1(H)	183.31±1(H)	1	1.1
12	-	183.31±1.8(H)	-	1	-
13	4	183.31±3(H)	183.31±3(H)	1	0.9
14	-	183.31±4.5(H)	-	1	-
15	5	183.31±7(H)	183.31±7(H)	1	0.9

Weighting functions of the MWHS and MWHS-2 water vapor channels calculated from the 1976 standard U.S. atmospheric profiles are shown in Fig. 1. Channels with frequencies centered around 183 GHz have their weighting functions distributed in the low and middle troposphere.

B. Brief Description of the RTM

The Community Radiative Transfer Model (CRTM) developed by the Joint Center for Satellite Data Assimilation (JCSDA) is used for the simulations of MWHS and MWHS-2 clear-sky radiances from ERA-interim reanalysis with an interval of 6 h (00, 06, 12, and 18 UTC) [24]–[26]. The version employed in this study is v2.2.3. The ERA-interim reanalysis has a horizontal resolution of 0.75° $\times$ 0.75° and 37 vertical levels in total, with the model top near 1 hPa. Profiles of atmospheric temperature, relative humidity, ozone mass mixing ratio, and pressure are required as input variables, along with surface parameters (e.g., surface skin temperature, surface pressure, 2-m dew point temperature, 2-m temperature, and 10-m winds) and information about the satellite geometry.

III. Model Simulations and Cloud Detection

Humidity sounding channels with different frequencies usually have different sensitivities to surface parameters, clouds, and precipitation. Although microwave radiation can penetrate some cirrus and nonprecipitating clouds, the absorption and scattering of precipitating and ice clouds still cannot be properly described by an RTM. In addition, surface emissivity also

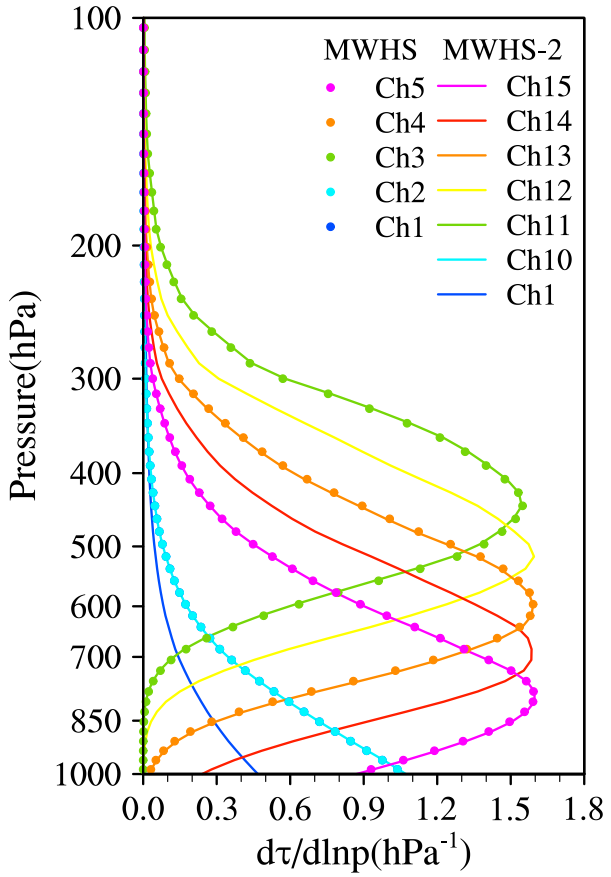

Fig. 1. Weighting functions of the MWHS and MWHS-2 humidity channels at the nadir.

contributes to the uncertainties in microwave radiance simulations, especially over land. To avoid the influence of these interfering factors, only clear-sky data over oceans between 55°S and 55°N are used to analyze the bias characteristics of different humidity sounders.

The liquid water path (LWP) and IWP products used to identify clear-sky MHS radiances are downloaded from NOAA's Comprehensive Large Array-Data Stewardship System (CLASS). These products are retrieved from NOAA-18 AMSU-A and MHS observations [27]–[29]. Those areas where both retrieved LWP and IWP are less than 0.05 kg/m2 are treated as clear-sky areas in this study. Also, the LWPs retrieved from AMSU-A are interpolated in MHS footprints. Fig. 2 shows the mean and standard deviations of O-B for NOAA-18 MHS channels 3–5 as a function of the beam position; only clear-sky data identified by LWP and IWP are used for the calculation from November 1 to 16, 2016. Nadir biases are 3.92, 3.10, and −0.44 K for channels 3–5, respectively. It can be seen that O-B biases of the MHS data vary smoothly with scan position and appear to be symmetric about the nadir for channel 5, but not for channels 3 and 4. The standard deviations of O-B are around 2 K for MHS channels 3 and 4, while channel 5 has a slightly larger standard deviation, especially at the edges of the scanline.

Unlike AMSU-A, the lack of two low-frequency window channels at 23.4 and 31.8 GHz that are sensitive to cloud liquid water makes it impossible to retrieve LWPs and IWPs from

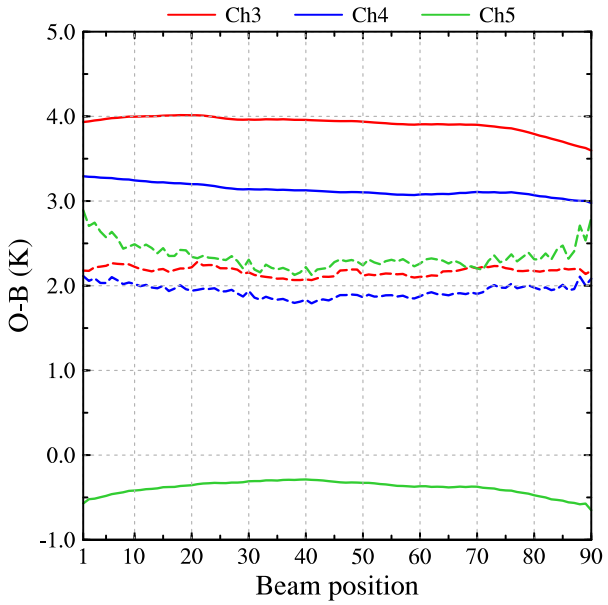

Fig. 2. Biases (solid curves) and standard deviations (dashed curves) of O-B varying with beam positions for NOAA-18 MHS channel 3 (red), 4 (blue), and 5 (green) clear-sky data identified by LWP/IWP retrieval products over the ocean between 55°S and 55°N from November 1 to 16, 2016.

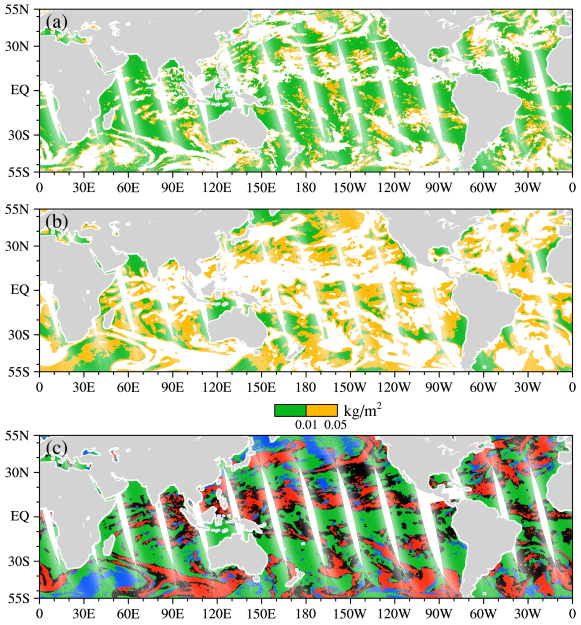

Fig. 3. Clear-sky data points over the ocean between 55°S and 55°N identified by (a) NOAA-18 AMSU-A LWP retrievals, (b) ERA-interim LWP reanalysis (green for LWP $<$ 0.01 kg/m^2 and yellow for 0.01 kg/m^2 $\leq$ LWP $\leq$ 0.05 kg/m^2), and (c) (green) clear-sky and (red) cloudy data points identified by both AMSU-A LWP products and ERA reanalysis, (blue) cloudy and (black) clear-sky data points identified by AMSU-A LWP products but not by ERA reanalysis for NOAA-18 MHS in ascending orbit on November 1, 2016.

MWHS or MWHS-2 observations. Therefore, it is necessary to find an alternative way to help identify clear-sky MWHS(-2) radiances. In this study, ERA-interim-derived LWP and IWP are used to identify cloudy observations. Fig. 3 shows the spatial distribution of MHS clear-sky data over the ocean, identified by AMSU-A LWP retrievals [Fig. 3(a)] and by

ERA LWP reanalysis [Fig. 3(b)] on November 1, 2016. Both AMSU-A LWP retrievals and ERA LWP are already interpolated in MHS footprints. Their differences are shown in Fig. 3(c), where data over clear skies and over cloudy areas identified by both AMSU-A LWP products and ERA LWP reanalysis are shown in green and red points, respectively; cloudy data identified only by retrieved products are shown in blue, and black points are for cloudy-sky data identified only by ERA LWP reanalysis. It can be seen that most clear-sky and cloudy observations identified by AMSU-A LWP retrievals can also be identified by ERA-derived LWP reanalysis. ERA LWP reanalysis only overestimated the water vapor contents at low latitudes and thus identified more cloudy data than the AMSU-A retrievals did. The situation is just the opposite in the middle or high latitudes. But, in general, the LWP of ERA reanalysis has a recognition ability very close to that of the retrieved LWP. Similar results can be derived from IWP patterns (figures omitted).

Fig. 4(a) shows the biases and standard deviations of O-B varying with beam position for the MHS data over a clear sky identified by ERA LWP and IWP. The characteristics of O-B biases and standard deviations in Fig. 4(a) are quite similar to those in Fig. 2. This proves again that the LWP and IWP from ERA data are good enough for the identification of cloudy data.

Fig. 4(b) shows the bias and standard deviations of O-B for five FY-3C MWHS-2 channels of FY-3C. Compared with MHS data, the scan-angle biases of the MWHS-2 data are larger than those of MHS. The mean biases with the nadir bias subtracted for the MHS channels are within the range of 0.5 K while the range is approximately 1.0 K for MWHS-2. The standard deviations of the MWHS-2 channels are around 2.0 K, which are similar to MHS channels 3 and 4, but slightly smaller than those of MHS channel 5. High-frequency oscillations of O-B biases can be observed along the scanline in all MWHS-2 humidity sounding channels. These oscillations (called "along-scanline noise" hereafter) also occur in the MWHS-2 oxygen absorption channels and MWHS on board FY-3A/B (figures omitted). In contrast, the O-B biases of the MHS channels are much smoother with respect to scan position. The cause of this oscillatory along-scanline noise still remains unclear; however, previous research has found that this noise has a periodicity of 2.6 FOVs according to power spectral density analysis [23].

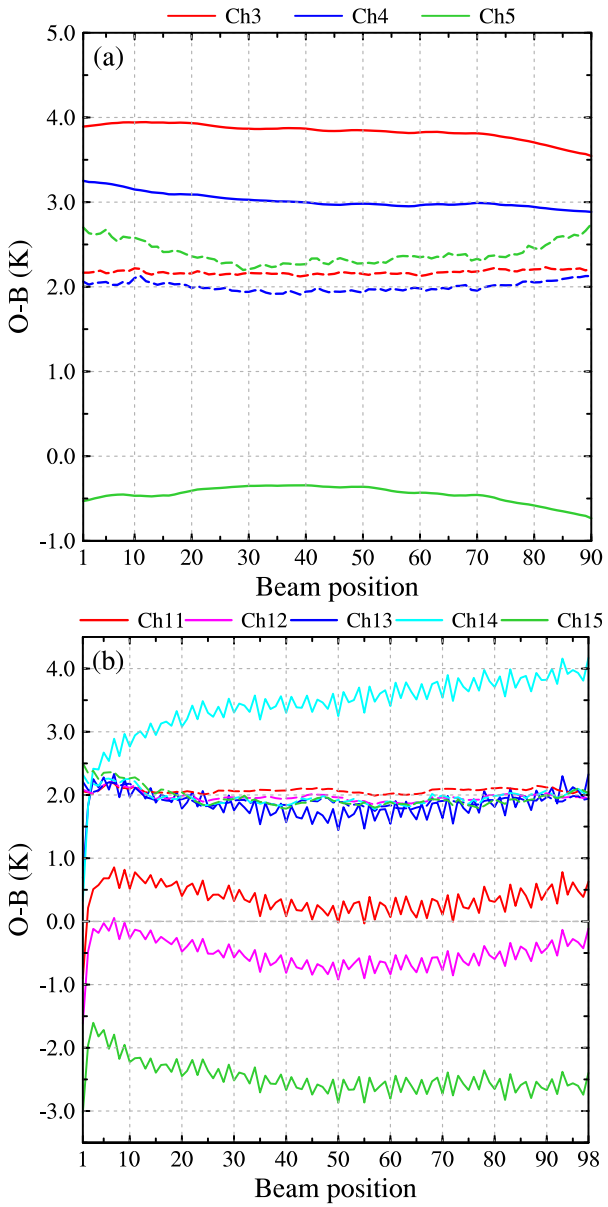

Fig. 4. Biases (solid curves) and standard deviations (dashed curves) of O-B varying with beam positions for (a) NOAA-18 MHS and (b) FY-3C MWHS-2 humidity sounding channel clear-sky data identified by LWP and IWP from the ERA reanalysis data set (LWP $\leq$ 0.05 kg/m^2 and IWP $\leq$ 0.05 kg/m^2) over the ocean between 55°S and 55°N.

IV. Filter and Analysis of MWHS Along-Scanline Noise

A. Brief Description of the PCA Method

The PCA method is a statistical procedure that can convert a set of possibly correlated variable values into linearly uncorrelated values. The PCA method was used in previous studies to remove and characterize random noise in hyperspectral infrared satellite observations and striping noise in some microwave instruments [30]–[35]. In this study, a PCA method combined with a five-point smoother is used to extract the along-scanline noise. First, PCA is carried out for a single swath of MWHS (or MWHS-2) observations.

A data matrix A is constructed from the brightness temperatures of the selected channel

$$A_{M\times N} = \begin{pmatrix} Tb_{1,1} & \cdots & Tb_{1,N} \\ \vdots & \ddots & \vdots \\ Tb_{M,1} & \cdots & Tb_{M,N} \end{pmatrix} \tag{1}$$

where $Tb_{k,j}$ $(k = 1, 2, \ldots, M; j = 1, 2, \ldots, N)$ is the observed brightness temperature at the kth FOV and the jth scan line of a single swath. M is the total number of FOVs on one scan line [98 for MWHS (MWHS-2)] and N is the number of scan lines.

Then, the scatter matrix S is computed from the following equation:

$$S = AA^T. \tag{2}$$

The eigenvalues $\lambda_i (i = 1, 2, \ldots, M)$ and eigenvectors $\vec{e}_i (i = 1, 2, \ldots, M)$ of matrix S are then calculated to satisfy the following equation:

$$S\vec{e} = \lambda\vec{e} \tag{3}$$

where $\vec{e}$ is called the principal component (PC) mode, which describes the variation in observations with FOV, and λ corresponds to the variance explained by the PC.

The eigenvector matrix E can be derived using (4) by sorting eigenvalues in descending order. Therefore, we have the following equation:

$$SE = E\Lambda \tag{4}$$

where

$$\Lambda = \begin{pmatrix} \lambda_1 & 0 & 0 \\ 0 & \ddots & 0 \\ 0 & 0 & \lambda_M \end{pmatrix}. \tag{5}$$

Since the values of $\vec{e}$ are orthonormal to each other, we have $E^{-1} = E^T$. The scatter matrix can be written as follows:

$$S = E\Lambda E^{-1} = E\Lambda E^T. \tag{6}$$

The data matrix A can be decomposed into: $A = EE^TA = EU$, where

$$U = E^TA = \begin{pmatrix} u_{1,1} & u_{1,2} & \cdots & u_{1,N} \\ u_{2,1} & u_{2,2} & \cdots & u_{2,N} \\ \vdots & \vdots & \ddots & \vdots \\ u_{M,1} & u_{M,2} & \cdots & u_{M,N} \end{pmatrix} = \begin{pmatrix} \vec{u}_1 \\ \vec{u}_2 \\ \vdots \\ \vec{u}_M \end{pmatrix} \tag{7}$$

is called the matrix of PC coefficients, indicating the along-track variation in the brightness temperature.

Then, a five-point smoothing (moving average) filter is applied to the first PC eigenvector ($\vec{e}_1$) to remove the along-scanline noise

$$\vec{e}^{\,sm}_{1,k} = \frac{1}{5}\sum_{i=-2}^{2} \vec{e}_{1,k+i} \tag{8}$$

where $\vec{e}^{\,sm}_{1,k}$ represents the smoothed $\vec{e}_1$ at the kth FOV.

Thus, the original observation matrix A can be rewritten in the form

$$A = \sum_{i=1}^{M} \vec{e}_i\vec{u}_i \tag{9}$$

in which $\vec{e}_i$ and $\vec{u}_i$ are the eigenvectors and the PC coefficients for the ith PC mode, respectively.

The observations can be reconstructed by replacing $\vec{e}_1$ with $\vec{e}^{\,sm}_1$

$$A^{\text{rec}} = \vec{e}^{\,sm}_1\vec{u}_1 + \sum_{i=2}^{M} \vec{e}_i\vec{u}_i \tag{10}$$

where $\vec{e}^{\,sm}_1$ is the five-point smoothed $\vec{e}_1$.

Finally, the noise is extracted by subtracting A^{rec} from A and the magnitude of mean noise for each channel is defined as

$$\text{noise}_m = \overline{|A - A^{rec}|}. \tag{11}$$

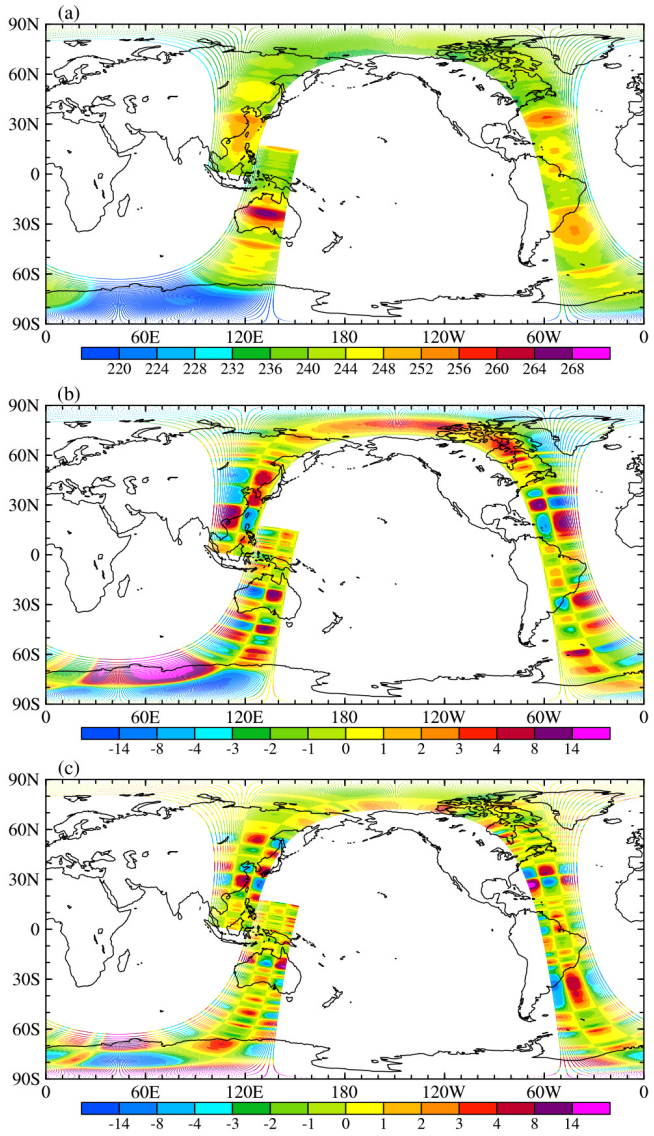

Fig. 5. Matrix of the vector products of PCs with PC coefficients ($\vec{e}_i\vec{u}_i$) for (a) first, (b) second, and (c) third modes of MWHS-2 channel 11 using a single swath at 0047-0229 UTC on November 1, 2013.

B. Characterization of MWHS-2 Noise Using PCA

The PCA method decomposes the brightness temperatures into uncorrelated PCs. Fig. 5 presents the spatial distributions of the products of the first three PCs with PC coefficients for a swath of MWHS-2 channel 11 observations at 0047–0229 UTC, November 1, 2013. The first PC mode contributed approximately 99.95% of the total variance, mainly indicating the average atmospheric state where the brightness temperature varies with latitude. In tropical or subtropical areas where water vapor is abundant, the scattering of clouds causes brightness temperatures to decrease. The optical path length decreases as the scan angle increases, which also results in observations varying with scan angle. This feature is well captured by the product of the first PCs with PC coefficients, as shown in Fig. 5(a). In the subsequent PC modes, the contribution of each PC to the total variance successively declines, accounting for 0.028% and 0.014% for

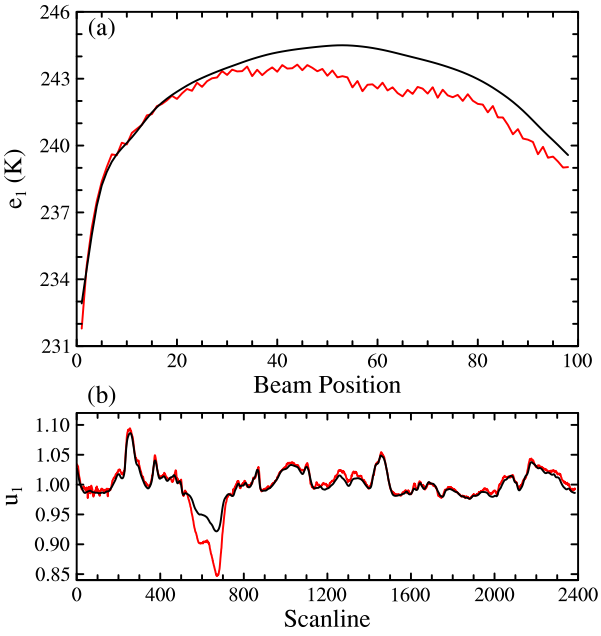

Fig. 6. First (a) eigenvector ($\vec{e_1}$) and (b) PC coefficients ($\vec{u_1}$) calculated from the (red) observed and (black) CRTM-simulated brightness temperatures for the same swath and channel as in Fig. 5.

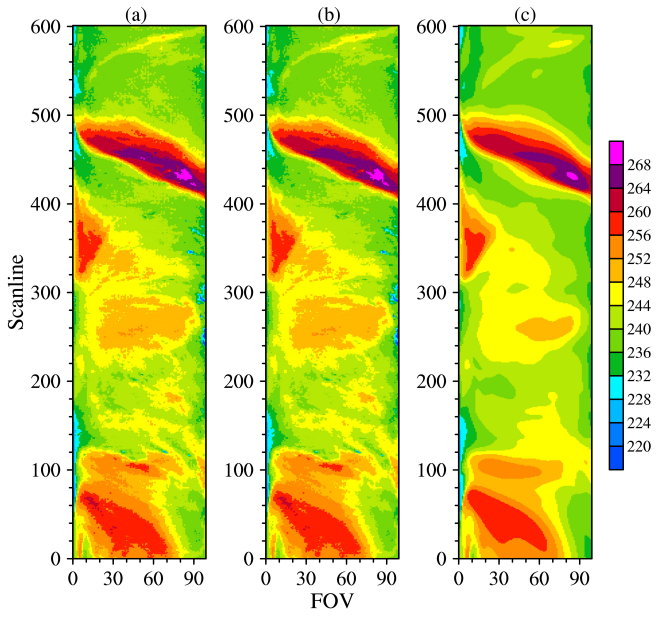

Fig. 7. Observed brightness temperatures (a) before and (b) after removing the along-scanline noises and (c) simulated brightness temperatures for MWHS-2 channel 11 using a chosen portion of the swath at 0047–0229 UTC on November 1, 2013.

the second and third PCs, respectively, representing some disturbances overlapping in the average state. These two PCs mainly describe the asymmetric and small-scale features with respect to the nadir.

The first eigenvector and its corresponding PC coefficient of the MWHS-2 channel 11 are given in Fig. 6 using the same swath as in Fig. 5. The variations of MWHS-2 observations (red solid curve) and model simulations (black solid curve) are in good agreement, and the limb effect is also simulated by CRTM. Since the first PC mode captures most of the scan-dependent features of cross-track radiometer measurements [23], the along-scanline noise is mainly contained in the PC coefficients corresponding to the first PC mode [see Fig. 6(a)]. Besides, the high-frequency noise in the first PC exists only in the MWHS-2 observations but cannot be simulated by the CRTM model.

A swath portion with 600 scanlines in the swath mentioned above is used to further characterize the noise in MWHS-2. The selected portion with 600 continuous scanlines covers an area of approximately 90° in the middle and low latitudes for MWHS-2 channel 11, whose weighting function peaks at approximately 450 hPa in a clear sky, is quite sensitive to the atmospheric temperature and water vapor. Therefore, brightness temperatures are easily affected by clouds and precipitation. Fig. 7(a) and (b) provides the observed and reconstructed brightness temperatures of the portion for MWHS-2 channel 11, respectively. The dynamic range of brightness temperatures of the MWHS-2 channel 11 is over 40 K. Since the magnitude of the along-scanline noise is much smaller than that of the observations, the differences between observed and reconstructed brightness temperatures can hardly be observed from Fig. 7(a)–(b). Fig. 7(c) is the distribution of model simulations for the same swath portion. The CRTM used in this article is accurate enough to simulate large-scale

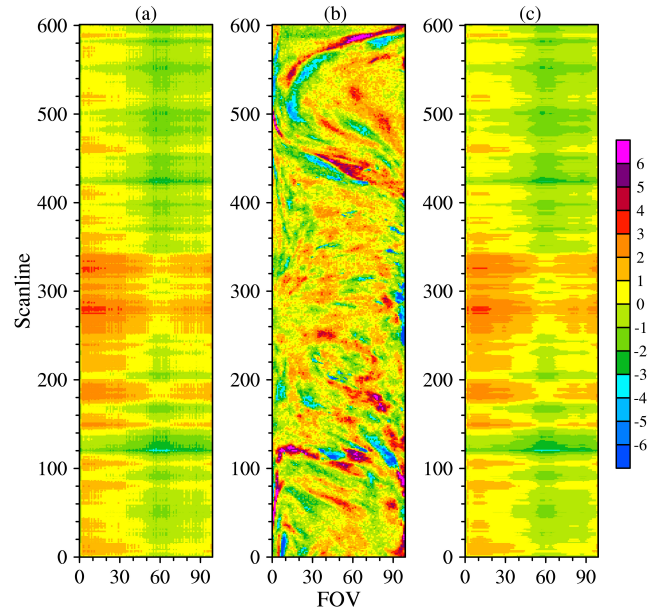

Fig. 8. (a) O-B of the first PC mode. (b) Sum of the last 97 PC modes. (c) Five-point smoothed O-Bs of the first mode for the same swath and channel as in Fig. 7.

features under clear-sky conditions, but cloud scattering and precipitation are not considered. Also, the errors in background temperature and water vapor profiles are another cause of the simulation errors.

Fig. 8(a) shows the difference between the observations and the simulations of the first PC mode of MWHS-2 channel 11. We can clearly see the noise along the scanline. Fig. 8(b) shows the O-Bs of the sum of the remaining 97 PCs for channel 11 and indicates the weather signals. The along-scanline noise does not occur in Fig. 8(b), which

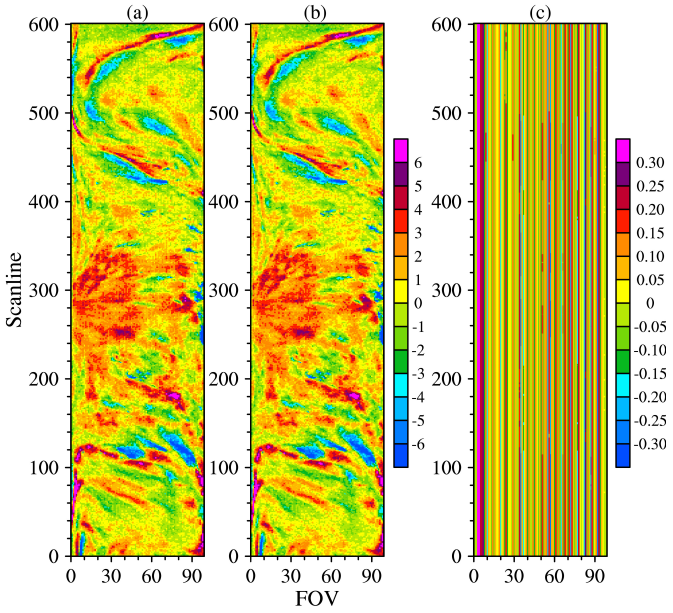

Fig. 9. O-B (a) before and (b) after removing the along-scanline noises and (c) along-scanline noises for the same swath and channel as in Fig. 7.

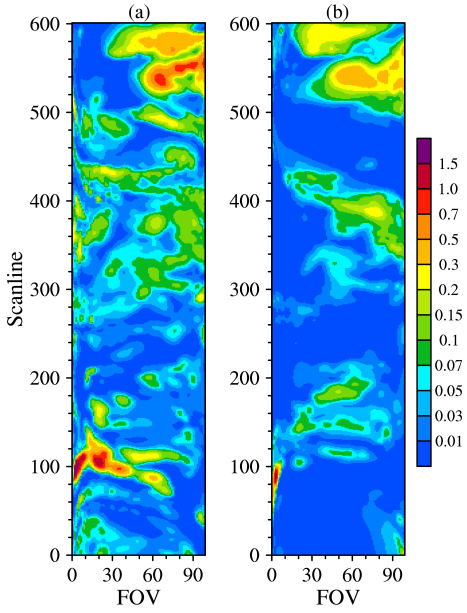

Fig. 10. Distributions of (a) LWP and (b) IWP of ERA reanalysis interpolated in MWHS-2 footprints for the same swath as in Fig. 7.

proves that this noise is mainly contained in the first PC mode. After applying a five-point smoothing filter to the observed brightness temperatures of the first PC, the O-Bs vary smoothly with FOV for the first PC [see Fig. 8(c)]. Fig. 9(a) and (b) shows the distribution of O-Bs before and after removing the along-scanline noise. The noise is obvious in O-B before it is removed from the observations, while the filtering operator can eliminate the discontinuity in the observed brightness temperatures, indicating that the noise is significantly reduced. Fig. 9(c) shows the distribution of the noise by subtracting the reconstructed brightness temperatures from the observations. The magnitude of this noise is within −0.3 to 0.3 K for most FOVs, which is much less than the NEdT for MWHS-2 channel 11. Notably, the magnitude of the noise has no relationship with the surface types and the noises vary only with FOVs as well as the first PC coefficient. In addition, we further examine whether the noise changes under cloudy conditions. From Fig. 10 which presents the ERA-derived LWP and IWP reanalysis that was interpolated in MWHS-2 footprints for the same swath as in Fig. 7, we can see that there are no significant differences between the noise under a clear sky and that under cloudy conditions [Fig. 9(c)]. Therefore, this method works in both clear and cloudy conditions.

Furthermore, this filtering method is applied to all five humidity channels of MWHS-2 to remove the along-scanline noise. In Fig. 11(a), the variations in O-B biases with respect to the FOVs for the five MWHS-2 humidity channels are shown. Biases before the filtering are shown as a gray curve, and biases with the noise removed are shown as colored curves. Nadir biases have already been subtracted. Only results from FOV 3 to 96 are given, since the brightness temperatures of the two FOVs at either end of a scanline remain the same after applying the five-point smoother. At the first few FOVs, the O-B biases increase rapidly for all channels except channel 14, then decrease gradually toward the nadir. The

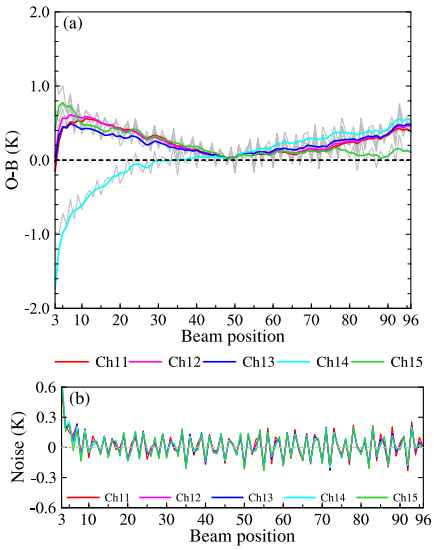

Fig. 11. Variations in (a) O-B biases and (b) averaged along-scanline noise with respect to beam position for FY-3C MWHS-2 channels 11–15. Gray and colored solid lines in Fig. 11(a) indicate data before and after PCA reconstruction, respectively.

O-B biases for the MWHS-2 channels show some symmetric features about the nadir, so that they increase as the scan angle ranges from 0 to 53.35°; for channel 14, its bias increases monotonously with scan position. These features did not change much, but biases vary more smoothly with FOVs after the filtering.

Fig. 11(b) shows the variation in mean noise with scan position. The noise for all channels is within the range of −0.3–0.3 K, and is not scan-angle dependent, but the variation seems to be highly correlated between channels.

C. Comparisons Between MWHS and MWHS-2

The along-scanline noises are contained in both MWHS and MWHS-2 on board the FY-3 polar-orbiting satellite. The

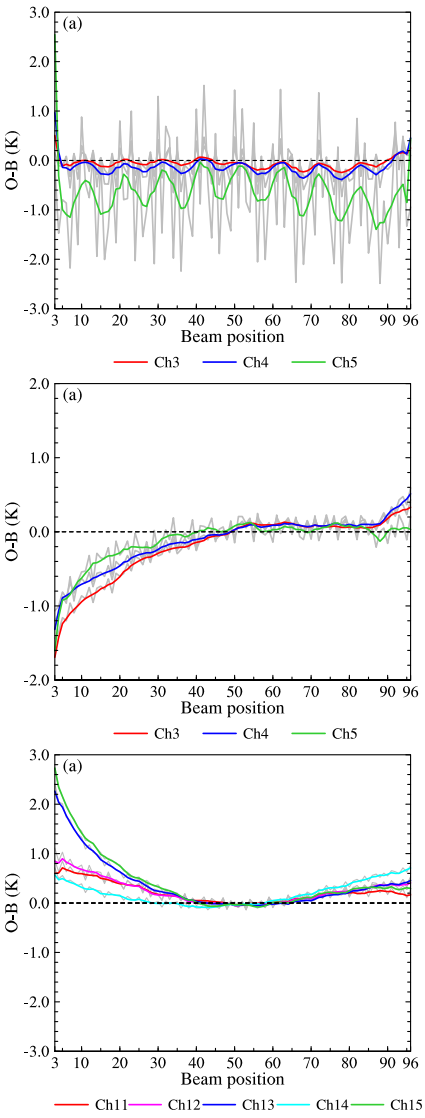

Fig. 12. Same as in Fig. 11(a) but for (a) FY-3A, (b) FY-3B MWHS, and (c) FY-3D MWHS-2 humidity sounding channels.

scan-angle dependence of the MWHS and MWHS-2 biases before and after smoothing are shown in Fig. 12. Observations used for statistics are from November 1 to 7, 2008 and from April 2 to 8, 2011 for FY-3A and FY-3B MWHS channels 3–5 [see Fig. 12(a) and (b)], and from June 1 to 7, 2018 for FY-3D MWHS-2 channels 11 to 15 [see Fig. 12(c)]. The O-B bias of FY-3A MWHS shows obvious fluctuation characteristics along the FOVs, especially for channel 5. The difference between the maximum and the minimum bias of FY-3A MWHS channel 5 reaches 4.0 K, which is much larger than those of other channels. After the noise is removed, it can be seen that the O-B biases of all FY-3A MWHS channels have a fluctuation characteristic with a period of about ten FOVs. The biases of the FY-3B and FY-3D channels show neither a sudden bend at the first few scanning positions as FY-3C does, nor periodic phenomena like those of FY-3A. The O-B biases of FY-3B MWHS increase with FOVs. The noise of the instrument on board FY-3B is much smaller than that of FY-3A and is comparable to the magnitude of the MWHS-2 noise. The O-B

TABLE II

MAGNITUDES OF ALONG-SCANLINE NOISES FOR MWHS AND MWHS-2 HUMIDITY SOUNDING CHANNELS

SATELLITE ID	Ch 11	Ch 12	Ch 13	Ch 14	Ch 15
FY-3A	0.16		0.27		0.89
FY-3B	0.06		0.07		0.12
FY-3C	0.11	0.10	0.11	0.12	0.12
FY-3D	0.07	0.07	0.06	0.06	0.06

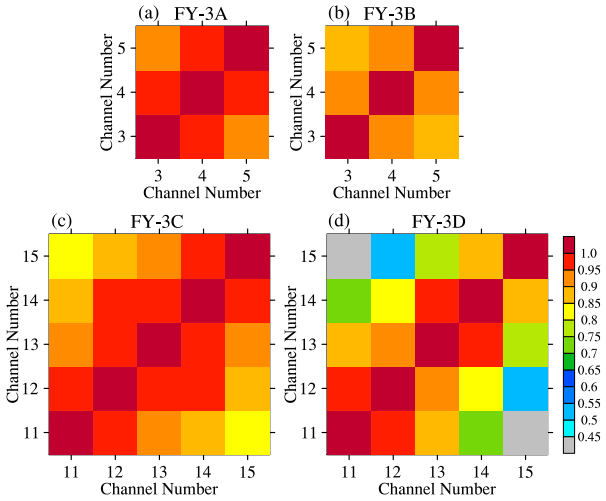

Fig. 13. Interchannel correlations of along-scanline noise for (a) FY-3A and (b) FY-3B MWHS and (c) FY-3C and (d) FY-3D MWHS-2 humidity sounding channels.

biases of FY-3D MWHS-2 have the most obvious symmetrical characteristics with the nadir.

Table II provides the magnitudes of the noise for different channels of MWHS and MWHS-2 on board FY-3 calculated from (11). The MWHS noise increases with the channel frequency except for FY-3D. FY-3A MWHS has the largest noise: 0.16, 0.27, and 0.89 K for channels 3–5, respectively. The noise of FY-3B MWHS is much smaller than the noise of FY-3A, especially for channel 5, where the noise is reduced from 0.89 to 0.12 K. All FY-3C MWHS-2 channels have noise around 0.11 K. The noise for FY-3D MWHS-2 is reduced to 0.06–0.07 K. With the continuous improvement in this instrument, this along-scanline noise has been significantly reduced.

As can be seen in Figs. 11 and 12, the along-scanline noise is highly consistent for different channels. This may contribute to the correlation in the MWHS observation errors. Fig. 13 shows the interchannel correlation coefficients of the along-scanline noises in the MWHS and MWHS-2 water vapor channels calculated using the one-week data described above. Generally, the noise in FY-3A, 3B, and 3C water vapor channels is strongly correlated between channels, but it is much weaker for FY-3D MWHS-2; weak correlation will contribute to the effective assimilation of these data.

V. SUMMARY

Satellite observations have become one of the most important sources for NWP and climate research. China has launched a series of polar-orbiting meteorological satellites (e.g., FY-3A/B/C/D) since 2008. Various instruments carried

on the Chinese Fengyun meteorological satellites provide numerous data for China's weather forecasting and climate research. More attention has been paid to the assimilation and climate applications of MWHS data. Therefore, it is very important to understand the bias characteristics of observations before they are used.

In this study, we compared the observed and simulated brightness temperatures of MWHS-2 and found along-scanline noises in the MWHS-2 observations. This noise is not significant in MHS on board the NOAA and MetOp series. To characterize and mitigate the along-scanline noises in MWHS-2, a PCA approach is first employed to decompose the observation data. The results show that this noise is mainly contained in the first PC mode. The O-B varies more smoothly with FOV after applying a five-point smoothing filter to the first PC. The noise can be effectively extracted and eliminated by the PCA/five-point smoothing method.

After the noise elimination, O-B biases for the MWHS-1/2 on board different Fengyun satellites are analyzed. There is a periodicity of 10 FOVs in the O-Bs of FY-3A MWHS. Biases for most channels of FY-3B, 3C, and 3D show asymmetric features with the nadir.

The along-scanline noise exists in both MWHS and MWHS-2 on board the FY-3 series. By comparing the noise of the four instruments, it is found that the noise in FY-3A MWHS is the largest, being 0.16, 0.27, and 0.89 K, for channels 3–5, respectively. Noise in FY-3 B/C/D is much smaller than that in FY-3A. Among them, the FY-3D MWHS-2 channels have the smallest noise at about 0.06 K.

There are also strong interchannel correlations between the noise of different channels except for FY-3D. A reduction in interchannel correlation of the noise will definitely be good for the effective assimilation of MWHS-2 observations.

Despite the fact that the PCA method combined with a five-point smoother can filter out the along-scanline noises, the current work does not examine the impact of quality-controlled data on NWP or other applications. Also, this study does not identify the root cause of the noise; these are goals in our follow-up study.

REFERENCES

[1] E. Andersson *et al.*, "Use of cloud-cleared radiances in three/four-dimensional variational data assimilation," *Quart. J. Roy. Meteorol. Soc.*, vol. 120, no. 517, pp. 627–653, Apr. 1994, doi: 10.1002/qj.49712051707.

[2] J. C. Derber and W.-S. Wu, "The use of TOVS cloud-cleared radiances in the NCEP SSI analysis system," *Monthly Weather Rev.*, vol. 126, no. 8, pp. 2287–2299, Aug. 1998.

[3] X. Zou, Z. Qin, and F. Weng, "Improved quantitative precipitation forecasts by MHS radiance data assimilation with a newly added cloud detection algorithm," *Monthly Weather Rev.*, vol. 141, no. 9, pp. 3203–3221, Sep. 2013.

[4] K. M. Newman, C. S. Schwartz, Z. Liu, H. Shao, and X.-Y. Huang, "Evaluating forecast impact of assimilating microwave humidity sounder (MHS) radiances with a regional ensemble Kalman filter data assimilation system," *Weather Forecasting*, vol. 30, no. 4, pp. 964–983, Aug. 2015.

[5] C. Dong *et al.*, "An overview of a new chinese weather satellite FY-3A," *Bull. Amer. Meteorol. Soc.*, vol. 90, no. 10, pp. 1531–1544, Oct. 2009.

[6] J. He, S. Zhang, and Z. Wang, "The retrievals and analysis of clear-sky water vapor density in the Arctic regions from MWHS measurements on FY-3A satellite," *Radio Sci.*, vol. 47, no. 2, pp. 301–311, 2012.

[7] J. He and S. Zhang, "Regional profiles and precipitation retrievals and analysis using FY-3C MWHTS," *Atmos. Climate Sci.*, vol. 6, no. 2, pp. 273–284, 2016.

[8] Y. Wang, Y. Fu, X. Fang, and Y. Zhang, "Estimating ice water path in tropical cyclones with multispectral microwave data from the FY-3B satellite," *IEEE Trans. Geosci. Remote Sens.*, vol. 52, no. 9, pp. 5548–5557, Sep. 2014.

[9] Y. Han, X. Zou, L. Lin, H. Yang, and F. Weng, "Cloud and precipitation features of Super Typhoon Neoguri revealed from dual oxygen absorption band sounding instruments on board FengYun-3C satellite," *Geophys. Res. Lett.*, vol. 42, no. 3, pp. 916–924, 2015, doi: 10.1002/2014GL062753.

[10] Z. Qin and X. Zou, "Uncertainty in fengyun-3C microwave humidity sounder measurements at 118 GHz with respect to simulations from GPS RO data," *IEEE Trans. Geosci. Remote Sens.*, vol. 54, no. 12, pp. 6907–6918, Dec. 2016.

[11] P. Dong, F. Weng, Q. Huang, Y. Han, and W. Han, "Estimation of cloud liquid water over oceans from dual oxygen absorption band to support the assimilation of second generation of microwave observation on board the chinese FY-3 satellite," *Int. J. Remote Sens.*, vol. 38, no. 18, pp. 5003–5021, Sep. 2017.

[12] P. Dong, J. Huang, G. Liu, and T, Zhang, "Assimilation of FY-3A microwave observations and simulation of brightness temperature under cloudy and rainy condition," *J. Trop. Meteorol.*, vol. 30, no. 2, pp. 302–310, 2014.

[13] D. Xu, J. Min, F. Shen, J. Ban, and P. Chen, "Assimilation of MWHS radiance data from the FY-3B satellite with the WRF hybrid-3DVAR system for the forecasting of binary typhoons," *J. Adv. Model. Earth Syst.*, vol. 8, no. 2, pp. 1014–1028, Jun. 2016, doi: 10.1002/2016MS000674.

[14] F. Carminati, B. Candy, W. Bell, and N. Atkinson, "Assessment and assimilation of FY-3 humidity sounders and imager in the UK met office global model," *Adv. Atmos. Sci.*, vol. 35, no. 8, pp. 942–954, Aug. 2018.

[15] Q. Lu, W. Bell, P. Bauer, N. Bormann, and C. Peubey, "An evaluation of FY-3A satellite data for numerical weather prediction," *Quart. J. Roy. Meteorol. Soc.*, vol. 137, no. 658, pp. 1298–1311, Jul. 2011.

[16] K. Chen, S. English, N. Bormann, and J. Zhu, "Assessment of FY-3A and FY-3B MWHS observations," *Weather Forecasting*, vol. 30, no. 5, pp. 1280–1290, Oct. 2015.

[17] K. Chen, N. Bormann, S. English, and J. Zhu, "Assimilation of Feng-Yun-3B satellite microwave humidity sounder data over land," *Adv. Atmos. Sci.*, vol. 35, no. 3, pp. 268–275, Mar. 2018.

[18] H. Lawrence, N. Bormann, A. J. Geer, Q. Lu, and S. J. English, "Evaluation and assimilation of the microwave sounder MWHS-2 onboard FY-3C in the ECMWF numerical weather prediction system," *IEEE Trans. Geosci. Remote Sens.*, vol. 56, no. 6, pp. 3333–3349, Jun. 2018.

[19] S. Gu, Y. Guo, Z. Wang, and N. Lu, "Calibration analyses for sounding channels of MWHS onboard FY-3A," *IEEE Trans. Geosci. Remote Sens.*, vol. 50, no. 12, pp. 4885–4891, Dec. 2012.

[20] H. Jieying, Z. Shengwei, and W. Zhenzhan, "Advanced microwave atmospheric sounder (AMAS) channel specifications and T/V calibration results on FY-3C satellite," *IEEE Trans. Geosci. Remote Sens.*, vol. 53, no. 1, pp. 481–493, Jan. 2015.

[21] J. Li, Z. Qin, and G. Liu, "A new generation of chinese FY-3C microwave sounding measurements and the initial assessments of its observations," *Int. J. Remote Sens.*, vol. 37, no. 17, pp. 4035–4058, Sep. 2016.

[22] Z. Wang *et al.*, "Performance analysis of microwave humidity and temperature sounder onboard the FY-3D satellite from prelaunch multiangle calibration data in thermal/vacuum test," *IEEE Trans. Geosci. Remote Sens.*, vol. 57, no. 3, pp. 1664–1683, Mar. 2019.

[23] X. Zou, Y. Ma, and Z. Qin, "Fengyun-3B MicroWave humidity sounder (MWHS) data noise characterization and filtering using principle component analysis," *IEEE Trans. Geosci. Remote Sens.*, vol. 50, no. 12, pp. 4892–4902, Dec. 2012.

[24] F. Weng, "Advances in radiative transfer modeling in support of satellite data assimilation," *J. Atmos. Sci.*, vol. 64, no. 11, pp. 3799–3807, Nov. 2007, doi: 10.1175/2007jas2112.1.

[25] Y. Han *et al.*, "JCSDA Community Radiative Transfer Model (CRTM)-Version 1," Nat. Ocean. Atmos. Admin. (NESDIS), Silver Spring, MD, USA, NOAA Tech. Rep. 122, 2006, p. 40.

[26] Y. Han *et al.*, "Current status of the JCSDA community radiative transfer model (CRTM)," in *Proc. 17th Int. ATOVS Study Conf.*, Monterey, CA, USA, 2010, pp. 1–20.

[27] F. Weng and N. C. Grody, "Retrieval of ice cloud parameters using a microwave imaging radiometer," *J. Atmos. Sci.*, vol. 57, no. 8, pp. 1069–1081, Apr. 2000.

[28] F. Weng, L. Zhao, R. R. Ferraro, G. Poe, X. Li, and N. C. Grody, "Advanced microwave sounding unit cloud and precipitation algorithms," *Radio Sci.*, vol. 38, no. 4, pp. 8086–8096, Jun. 2003.
[29] L. Zhao and F. Weng, "Retrieval of ice cloud parameters using the advanced microwave sounding unit," *J. Appl. Meteorol.*, vol. 41, no. 4, pp. 384–395, Apr. 2002.
[30] D. D. Turner, R. O. Knuteson, H. E. Revercomb, C. Lo, and R. G. Dedecker, "Noise reduction of atmospheric emitted radiance interferometer (AERI) observations using principal component analysis," *J. Atmos. Ocean. Technol.*, vol. 23, no. 9, pp. 1223–1238, Sep. 2006.
[31] D. C. Tobin *et al.*, "Hyperspectral data noise characterization using principle component analysis: application to the atmospheric infrared sounder," *J. Appl. Remote Sens.*, vol. 1, no. 1, pp. 341–353, 2007.
[32] D. C. Tobin, H. E. Revercomb, and P. Antonelli, "Principal component analysis of IASI spectra with a focus on non-uniform scene effects on the ILS," in *Proc. AIP Conf.*, 2009, p. 1100.
[33] Z. Qin, X. Zou and F. Weng, "Analysis of ATMS striping noise from its Earth scene observations," *J. Geophys. Res., Atmos.*, vol. 118, no. 13, pp. 13214–13229, 2013.
[34] Y. Ma and X. Zou, "Striping noise mitigation in ATMS brightness temperatures and its impact on cloud LWP retrievals," *J. Geophys. Res., Atmos.*, vol. 120, no. 13, pp. 6634–6653, Jul. 2015.
[35] X. Zou, H. Dong, and Z. Qin, "Striping noise reduction for ATMS window channels using a modified destriping algorithm," *Quart. J. Roy. Meteorol. Soc.*, vol. 143, no. 707, pp. 2567–2577, Jul. 2017.

Lijian Zhu received the B.S. and M.S. degrees in meteorology from the Nanjing University of Information Science and Technology (NUIST), Nanjing, China, in 2015 and 2018, respectively, where he is pursuing the Ph.D. degree.

He is also a Visiting Scholar at the Center for Analysis and Prediction of Storms (CAPS), University of Oklahoma, Norman, OK, USA. His research interests include satellite remote sensing and data assimilation.

Zhengkun Qin received the B.S. degree in mathematics and the Ph.D. degree in meteorology from the Nanjing University of Information Science and Technology (NUIST), Nanjing, China, in 2001 and 2007, respectively.

From 2009 to 2014, he was a Visiting Scholar with the Department of Earth, Ocean, and Atmospheric Science, Florida State University, Tallahassee, FL, USA. He is a Full Professor with the Joint Center of Data Assimilation for Research and Application, NUIST. Since 2016, he has been a Visiting Scholar with the Earth System Science Interdisciplinary Center, University of Maryland at College Park, College Park, MD, USA. His research interests include satellite radiance data assimilation, surface data quality control, and the study of nonlinear climate trend using satellite data.

Jinzhong Min received the B.S. and Ph.D. degrees from the Nanjing Institute of Meteorology, Nanjing, China, in 1988 and 2000, respectively.

From March 2002 to May 2003, he was a Senior Visiting Scholar with the Center for Analysis and Prediction of Storms (CAPS), University of Oklahoma, Norman, OK, USA. From 2012 to 2014, he worked as the Dean of the College of Atmospheric Sciences, the Director of the Key Laboratory of Ministry of Meteorological Disaster Education, and the Executive Director of the Meteorology Department, Nanjing University of Information Science and Technology, Nanjing. He is mainly involved in the research of small- and medium-scale numerical simulation and data assimilation, storm scale ensemble forecasting, climate change, and regional response.

Ming Xue received the B.S. degree in meteorology from Nanjing University, Nanjing, China, in 1984, and the Ph.D. degree in meteorology from Reading University, Reading, U.K., in 1989, under the supervision of Prof. Alan Thorpe.

In 1989, he joined the Center for Analysis and Prediction of Storms (CAPS), University of Oklahoma, Norman, OK, USA, as a Post-Doctoral Fellow and became a Senior Research Scientist in 1993. He is the Principal Architect of the Advanced Regional Prediction System (ARPS), which won the Discover Magazine Award for Technology Innovation (computer software category) and the Computerworld Smithsonian Award (science category) in 1997. He is the Analysis and Prediction Thrust Leader, Associate Director, and University of Oklahoma PI of the NSF Engineering Research Center (ERC) for Collaborative Adaptive Sensing of the Atmosphere (CASA). He is a Professor of the School of Meteorology and the Director of CAPS. His main research interests involve the development of advanced numerical modeling and data assimilation systems, numerical weather prediction, high-performance computing, simulation and prediction of mesoscale and convective scale systems, mesoscale and storm-scale dynamics, tornado dynamics, data assimilation and predictability, and variational and ensemble Kalman filter techniques for assimilating radar data.